Dependence of the electronic structure of the EuS/InAs interface on the bonding configuration

Maituo Yu,[1] Saeed Moayedpour,[2] Shuyang Yang,[1] Derek Dardzinski,[1] Chunzhi Wu,[3] Vlad S. Pribiag,[4] and Noa Marom[1,2,5,*]

[1]*Department of Materials Science and Engineering, Carnegie Mellon University, Pittsburgh, Pennsylvania 15213, USA*
[2]*Department of Chemistry, Carnegie Mellon University, Pittsburgh, Pennsylvania 15213, USA*
[3]*Department of Civil and Environmental Engineering, Carnegie Mellon University, Pittsburgh, Pennsylvania 15213, USA*
[4]*School of Physics and Astronomy, University of Minnesota, Minneapolis, Minnesota 55455, USA*
[5]*Department of Physics, Carnegie Mellon University, Pittsburgh, Pennsylvania 15213, USA*

(Received 4 April 2021; accepted 14 June 2021; published 29 June 2021)

Recently, the EuS/InAs interface has attracted attention for the possibility of inducing magnetic exchange correlations in a strong spin-orbit semiconductor, which could be useful for topological quantum devices. We use density functional theory with a machine-learned Hubbard U correction [Yu *et al.*, npj Comput. Mater. **6**, 180 (2020)] to elucidate the effect of the bonding configuration at the interface on the electronic structure. For all interface configurations considered here, we find that the EuS valence band maximum (VBM) lies below the InAs VBM. In addition, dispersed states emerge at the top of the InAs VBM at the interface, which do not exist in either material separately. These states are contributed mainly by the InAs layer adjacent to the interface. They are localized at the interface and may be attributed to charge transfer from the EuS to the InAs. The interface configuration affects the position of the EuS VBM with respect to the InAs VBM, as well as the dispersion of the interface states. For all interface configurations studied here, the induced magnetic moment in the InAs is small. Our results suggest that this interface, in its coherent form studied here, may not be promising for inducing equilibrium magnetic properties in InAs.

DOI: 10.1103/PhysRevMaterials.5.064606

I. INTRODUCTION

Majorana zero modes may provide a pathway to the realization of fault-tolerant quantum computing schemes [1–6]. Several types of hybrid materials systems have been proposed to produce Majorana zero modes. These include the surface of a three-dimensional (3D) topological insulator and two- or one-dimensional semiconductors with strong spin-orbit coupling, in each case interfaced with an s-wave superconductor [4,7–11]. To induce superconductivity at the interface, the semiconductor is in contact with a superconductor, such as Al, Pb, and Nb [12–16]. One challenge that may be encountered in such platforms is that a large magnetic field is required to drive the system into the topological regime, which may be detrimental to the superconductivity [10,17–19]. A possible solution is to add a ferromagnet (FM) in contact with the semiconductor to induce magnetism in the semiconductor internally via nonequilibrium spin injection [20], stray fields [21], or the magnetic proximity effect, thus obviating the need for an external magnetic field [22].

FM/semiconductor heterostructures have been widely used for spintronics [23–25]. Typically, the FM is a metal, such as Fe, Ni, or Co [26–28]. However, a metallic FM may induce undesirable states in the gap of a semiconductor and can have detrimental effects by shunting away the current in a hybrid device. A ferromagnetic insulator (FMI) may be advantageous for Majorana devices if it provides proximity-induced magnetism in the semiconductor without introducing such deleterious effects [29]. Europium-containing FMIs have a particularly high magnetic moment per Eu atom and a large exchange coupling [30]. Several studies have reported proximity-induced magnetism in various materials in contact with europium oxide and europium chalcogenides, including the EuS/Bi_2Se_3 interface [31], phosphorene on EuO [32], MoS_2-EuS heterojunctions [33], and EuS/Al heterostructures [34–37]. A strong interfacial exchange field has been detected at the EuS/Pt interface [38]. Moreover, proximity to EuS may break the time-reversal symmetry and open a gap in the interface state of topological insulators [39–41].

EuS has a rocksalt structure with less than 1% lattice mismatch to InAs, which makes it favorable for epitaxial growth. Therefore, the EuS/InAs interface could be an ideal option for a hybrid FMI-semiconductor-superconductor structure if the proximity-induced magnetism in the InAs is sufficiently strong. Recently, an epitaxial EuS/InAs interface with a (001) orientation has been grown and characterized [42]. Angle-resolved photoemission spectroscopy (ARPES) has shown that the Eu $4f$ states, which form the top of the valence manifold of EuS, lie below the valence band maximum of InAs and that an interfacial quantum well state forms in the InAs. However, proximity-induced magnetism in the InAs could not be detected in neutron and x-ray reflectivity measurements. Based on these null results, it was concluded in Ref. [42] that the magnetic proximity effect at the EuS/InAs interface is weak and has a small influence on the overall

*nmarom@andrew.cmu.edu

 ©2021 American Physical Society

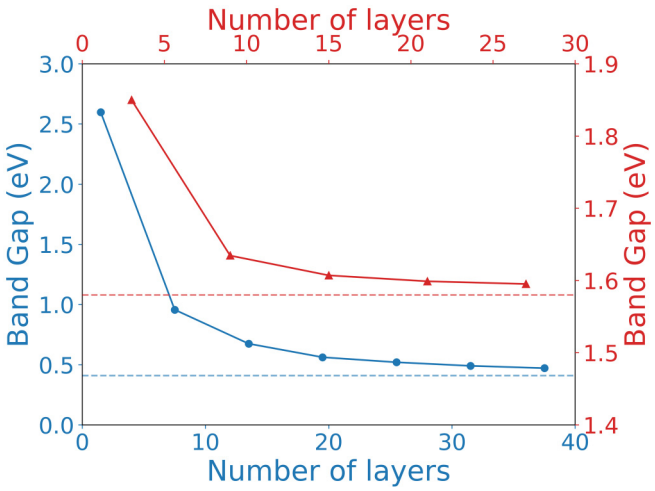

FIG. 1. The band gap of InAs (blue) and EuS (red) slabs as a function of the number of atomic layers. Dashed lines denote the bulk limit of 0.41 eV for InAs and 1.58 eV for EuS.

magnetism in InAs. Subsequent work on a hybrid structure of InAs nanowires, Al, and EuS, in which the EuS was in contact with both InAs and Al, argued for the presence of magnetic exchange effects [43]. Very recently, zero-bias peaks, which are a signature of topological superconductivity, have been reported in such a hybrid structure [44]. However, these observations could be attributed to distinct mechanisms, such as the EuS inducing magnetism in Al [34,36], rather than the InAs or changing stray magnetic fields during the complex magnetic reversal [20].

To elucidate the electronic structure of the EuS/InAs interface and help resolve the question of whether and to what extent proximity-induced magnetism is achieved in the InAs, we conduct first-principles simulations within density functional theory (DFT). A challenge for DFT simulations of the EuS/InAs interface is that commonly used semilocal exchange-correlation functionals, such as the generalized gradient approximation of Perdew, Burke, and Ernzerhof (PBE) [45], provide a poor description of EuS and InAs, producing no band gap for both materials [46–49]. A more accurate description may be provided by hybrid functionals, which contain a fraction of exact exchange [50,51]. However, hybrid functionals are impractical for simulations of large interface models, owing to their high computational cost. Alternatively, within the DFT+U approach [52,53], a Hubbard U correction may be added to a semilocal DFT functional, such as the PBE functional. Recently, we developed a method of machine learning the optimal value of the effective Hubbard U parameter by Bayesian optimization (BO) [46]. The PBE+U(BO) method has been demonstrated to provide a reliable description of bulk EuS and InAs [46], as well as InAs surfaces [54] and interfaces [55]. Here, we use PBE+U(BO) to study the electronic structure of the EuS/InAs (001) interface. The bonding configuration at the interface may significantly affect the electronic and magnetic properties [56]; therefore, we consider different interface configurations.

We find that the interface configurations studied here share qualitatively similar electronic and magnetic properties. However, the quantitative details differ between configurations. In all interface configurations the valance band maximum (VBM) of EuS lies below the VBM of InAs, and a dispersed interface state emerges, in agreement with the ARPES experiments reported in Ref. [42]. The interface configuration affects the extent of charge transfer from EuS to InAs and, as a result, the band alignment between EuS and InAs, as well as the interface state dispersion. Greater charge transfer pushes the EuS VBM lower with respect to the InAs VBM and leads to more dispersed interface states. In all configurations studied here, the induced magnetic moment in the InAs is found to be small and spatially confined to the vicinity of the interface, which is also in agreement with Ref. [42]. Our results suggest that the EuS/InAs interface, in its coherent form, is not particularly well suited for inducing magnetic exchange correlations in InAs.

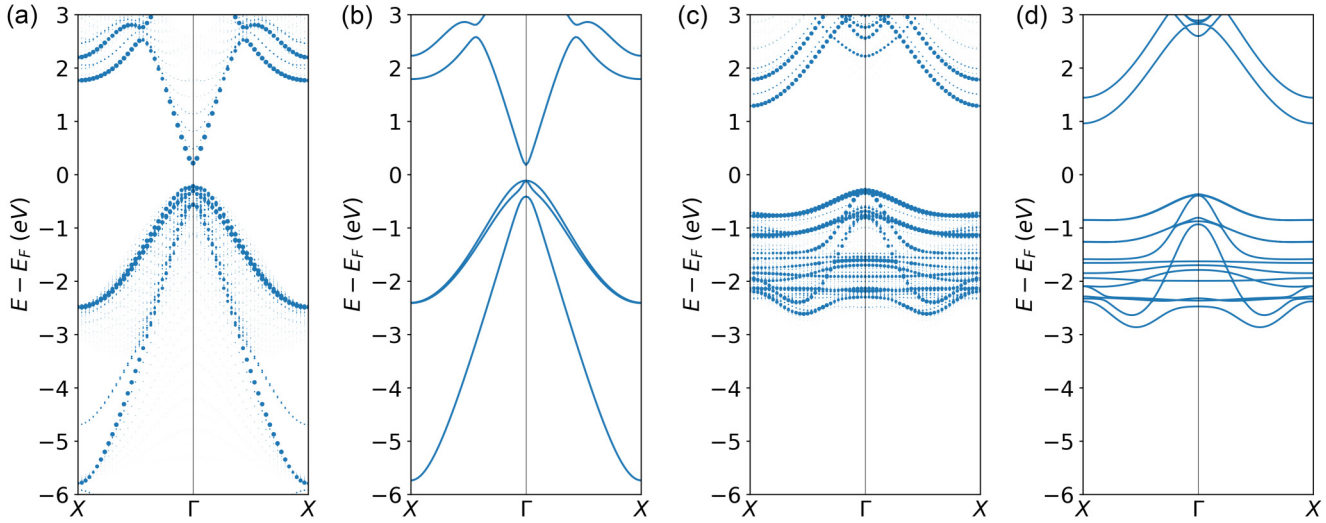

FIG. 2. (a) Bulk unfolded band structure of an InAs slab with 75 layers compared to (b) the band structure of bulk InAs oriented in the (001) direction. (c) Bulk unfolded band structure of a EuS slab with 21 layers compared to (d) the band structure of bulk EuS oriented in the (001) direction.

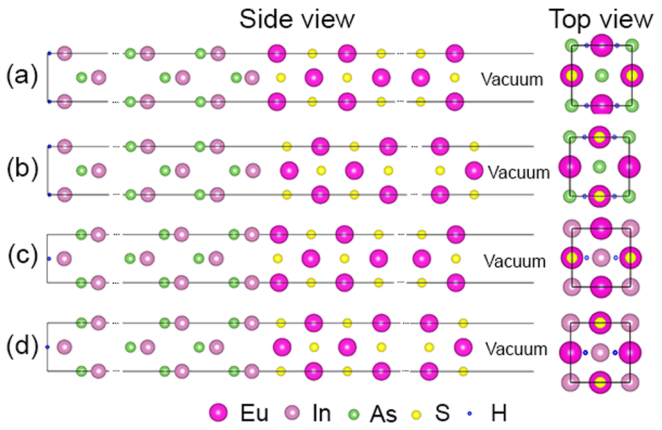

FIG. 3. Side view and top view of four configurations of an ideal EuS/InAs interface. From top to bottom, the configurations are labeled as (a) configuration 1 (C1), (b) configuration 2 (C2), (c) configuration 3 (C3), and (d) configuration 4 (C4).

II. METHODS

DFT calculations were performed using the Vienna Ab initio Simulation Package (VASP) with the projector augmented wave method [57–59]. PBE+U was used to describe the exchange-correlation interactions among electrons. The Hubbard U correction was applied within the Dudarev approach [53] to the p orbitals of In and As and the f orbitals of Eu. The effective U parameters, $U_{eff} = U - J$, which correspond to the difference between the on-site Coulomb interaction U and the exchange interaction J, were machine learned by BO, as described in Ref. [46]. The U_{eff} values obtained therein were $U_{eff}^{In,p} = -0.5\,\text{eV}$, $U_{eff}^{As,p} = -7.5\,\text{eV}$, and $U_{eff}^{Eu,f} = 8.4\,\text{eV}$. The PBE+$U$(BO) method with these parameters was used successfully for InAs surfaces [54] and the InAs/GaSb interface [55]. A plane-wave basis set was used with a kinetic energy cutoff of 450 eV. The Brillouin zone was sampled using the Monkhorst-Pack scheme with an $8 \times 8 \times 1$ k-point mesh. Spin-orbit coupling (SOC) [60] was included in all calculations with the z spin quantization axis, as well as the dipole correction [61]. To avoid spurious interactions between periodic replicas in slab models, a sufficiently large vacuum region of ∼40 Å was added in the z direction. To eliminate surface states due to dangling bonds, the InAs slab was passivated by pseudohydrogen atoms with 1.25 electrons. In the structural relaxation and the interfacial distance optimization, the Tkatchenko-Scheffler pairwise dispersion method [62] was used to describe the van der Waals interactions between the EuS film and the InAs substrate. The convergence criterion used in the structural relaxation was for the Hellman-Feynman forces acting on ions to be below 0.01 eV/Å. Bulk band unfolding [54] was applied to all band structures to project the slab band structure onto the primitive cell and facilitate comparison with ARPES experiments. The spin-polarized density of states (DOS) of calculations with SOC was plotted by extracting the DOS of the majority-spin channels and minority spin channels along the easy axis.

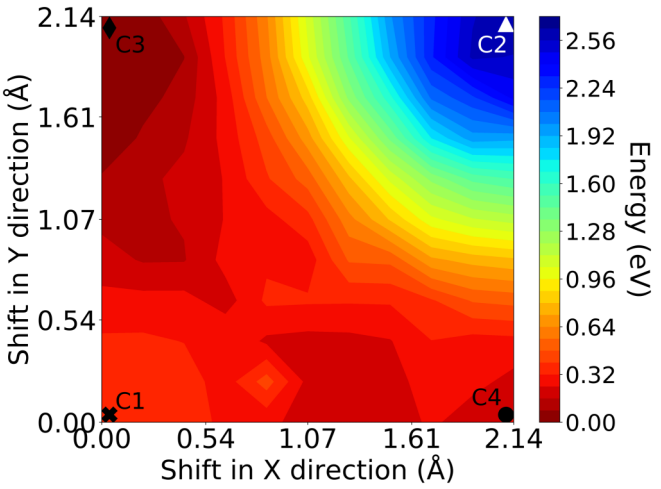

FIG. 5. PES scan at the interfacial distance of 2.4 Å

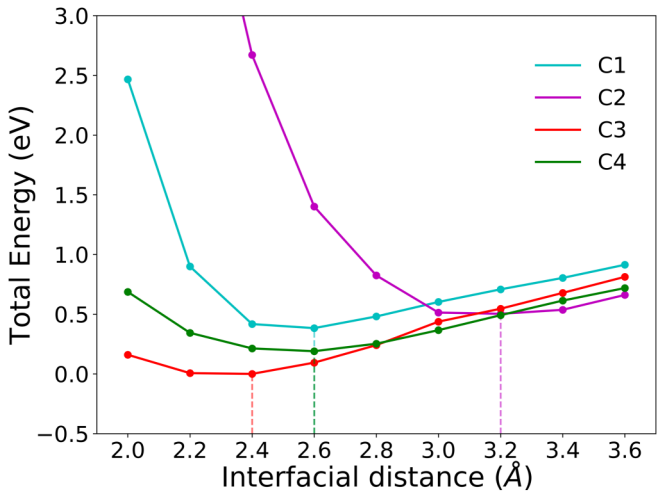

FIG. 4. Total energy change as a function of the interfacial distance for the four interface configurations. The lowest minimum is referenced to zero.

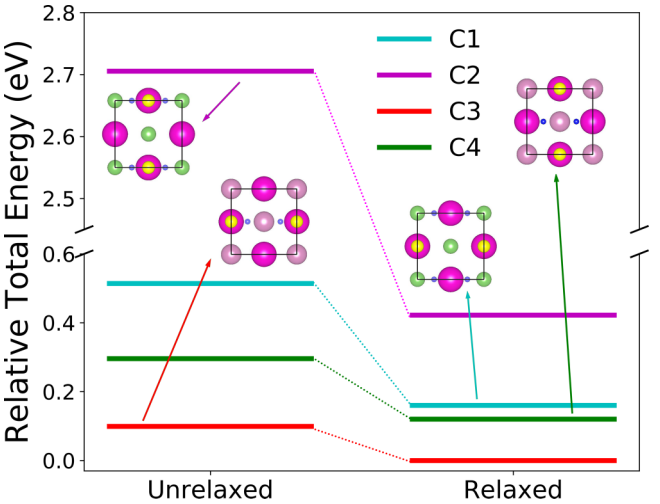

FIG. 6. Energy ranking of the four interface configurations before and after relaxation. The lowest -energy structure after relaxation is referenced to zero.

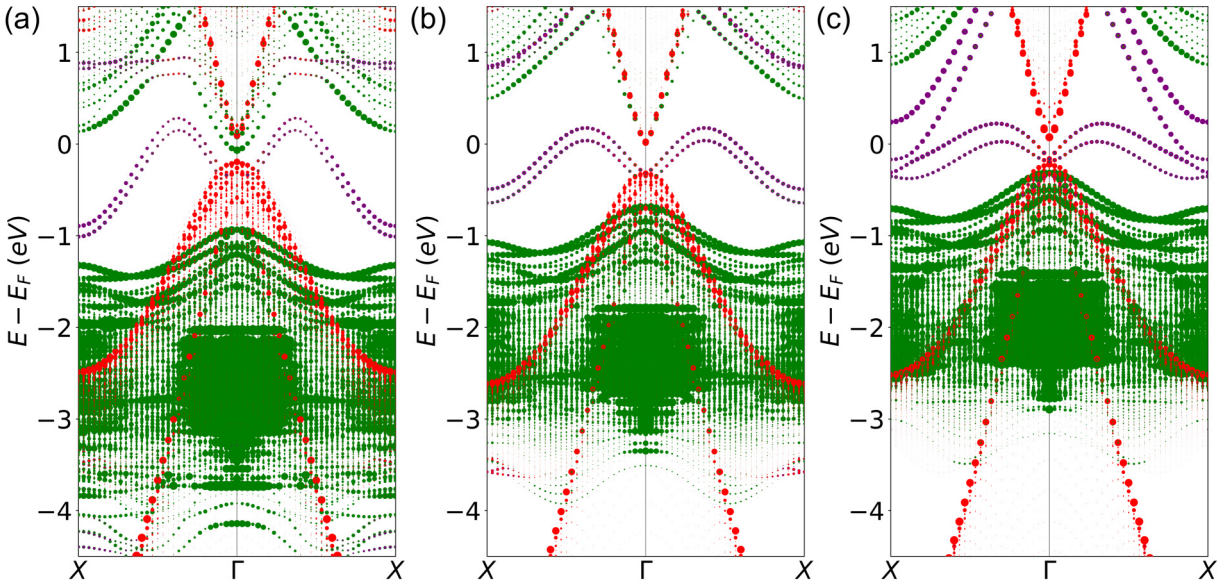

FIG. 7. Unfolded band structure of different interface configurations: (a) C1, (b) C3, and (c) C4. The red, green, and purple markers denote the contributions from InAs, EuS, and the interface states, respectively.

III. RESULTS AND DISCUSSION

We begin by studying the band structures of InAs(001) and EuS(001) slabs separately. Owing to the effect of quantum confinement, the band gap of a slab model decreases as the number of layers increases, eventually approaching the bulk band gap, as shown in Fig. 1. The band gap of InAs converges with 75 atomic layers, and the band gap of EuS converges with 21 atomic layers. The bulk-unfolded band structures of these slab models of InAs and EuS are compared to bulk band structures with a (001) orientation in Fig. 2. With this number of layers the band gap of InAs is 0.02 eV larger than the bulk limit, and the band gap of EuS is 0.22 eV larger than the bulk limit. The main features of the bulk band structure are reproduced well by the slab models.

To model the EuS/InAs interface, we assumed that an epitaxially matched EuS film would grow on top of In-terminated InAs(001) based on the experiments reported in Ref. [42]. Therefore, the lattice constant of the InAs substrate was fixed at 6.06 Å, and the EuS film was strained to match it. Four unique interface configurations are possible with the EuS atoms positioned directly above the InAs lattice sites, as shown in Figs. 3(a)–3(d). In Ref. [42] configuration 1 [C1; shown in Fig. 3(a)] was proposed based on high-angle annular dark-field (HAADF) imaging using an aberration-corrected scanning transmission electron microscope (AC-STEM). It was also noted therein that single-layer intermixing caused a displacement from ideal atomic rows and that atomic steps were likely present at the interface. Here, we consider only ideal interfaces. Intermixing, atomic steps, and the possible coexistence of different interface configurations are not taken into account.

To determine the interfacial distance to use as a starting point for relaxation for each configuration, the EuS film was moved along the z direction with respect to the InAs substrate with a step size of 0.1 Å. The resulting energy curves are shown in Fig. 4. We find that the interface configuration significantly affects the interfacial distance. The largest interfacial distance of 3.2 Å is found for configuration 2 (C2), and the smallest interfacial distance of 2.4 Å is found for configuration 3 (C3).

A potential energy surface (PES) scan was performed by shifting the EuS film in the xy plane at a fixed distance of 2.4 Å from the InAs substrate along z. The PES scan was performed with 11 layers of InAs and 3 layers of EuS. We performed a convergence test with a varying number of layers of InAs and EuS to verify that the energy ranking exhibited in the PES is not affected by the number of layers. The resulting PES is shown in Fig. 5. C3 is the global minimum. Configuration 4 (C4) is a local minimum. C2 is the global maximum. Based on our calculations, C1, reported in Ref. [42], is, in fact, a local maximum.

Starting from the optimal interfacial distance obtained for each configuration, geometry relaxation was performed for the first six InAs layers and two EuS layers around the interface. The atomic positions were constrained in the xy plane and allowed to vary in the z direction. Figure 6 shows the relative energy ranking of the four configurations before and after relaxation. Relaxation resulted in the reduction of the energies of all structures; however, it did not affect the stability ranking. After relaxation, C3 is still the most stable, followed by C4, C1, and C2. C2 is the least stable owing to unfavorable cation-cation bonding at the interface. The higher stability of C3 and C4 may be attributed to the tetrahedral site being favored over the edge-center site because it matches better the zinc-blende packing of InAs. The HAADF-STEM micrograph of the EuS/InAs interface shown in Ref. [42] could also be compatible with the C3 model in terms of atomic positions. However, a more complex 3D structure including, for example, surface atomic steps would be needed to explain the HAADF intensity reduction and atomic column elongation in the positions near the interface for a full

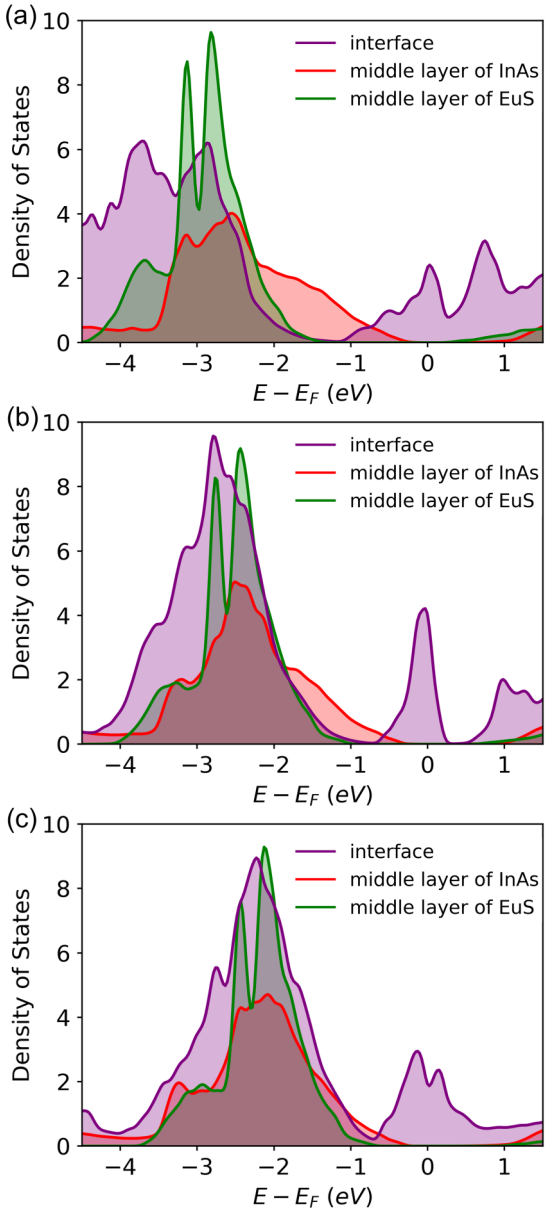

FIG. 8. Local density of states of (a) C1, (b) C3, and (c) C4. The interface layer refers to the first InAs and EuS layers at the interface. The middle layer of InAs refers to the 38th InAs layer from the interface. The middle layer of EuS refers to the 11th EuS layer from the interface. The Fermi level is shifted to 0 eV.

matching of the experimental image with the C3 epitaxial arrangement.

We now proceed to examine the effect of the atomistic configuration of the interface on its electronic structure. Because C2 is unstable we do not consider it further. C1 is considered despite being a local maximum because it was proposed in Ref. [42]. Figure 7 shows bulk-unfolded band structures of C1, C3, and C4. For all three configurations the top of the EuS valence band (green) is positioned below the top of the InAs valence band (red) at the Γ point, in agreement with the ARPES results from Ref. [42]. However, the interface configuration significantly affects the band alignment: For C1, the EuS VBM is found 0.72 eV below the InAs VBM; for C3,

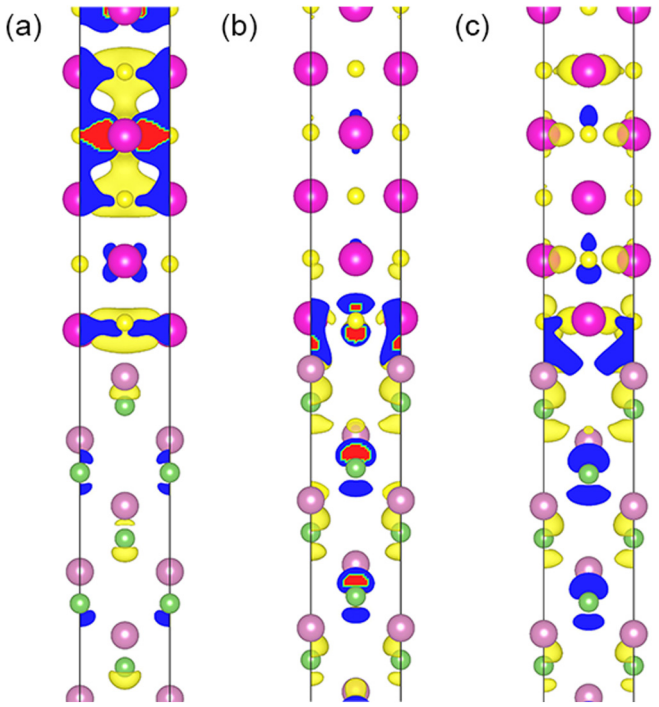

FIG. 9. The partial charges associated with the interface states of (a) C1, (b) C3, and (c) C4 at the Γ point. The electron charge isosurface is shown in yellow. Cross sections of the isosurface that intersect with the unit cell boundary are colored in blue, and hollow cavities within the isosurface that intersect with the unit cell boundary are shown in red.

the EuS VBM is found 0.36 eV below the InAs VBM; and for C4 it is found 0.09 eV below the InAs VBM. The band alignment produced by C3 appears to be in better agreement with the ARPES results from Ref. [42] than C1. Additional calculations of the valence band offsets using the macroscopic averaging procedure [63,64] instead of the band structure are provided in the Supplemental Material [65].

Interestingly, dispersed states, colored in purple in Fig. 7, appear at the top of the valence band at the EuS/InAs interface that are not present in either InAs or EuS alone (see Fig. 2). By resolving the atomic contributions to the band structure, we find that these interface states are contributed predominantly by the first InAs layer at the interface. The interface states found here are in agreement with the quantum well state observed in ARPES in Ref. [42]. The dispersion of the interface states depends on the interface configuration, with C1 producing the greatest band dispersion and C4 yielding the smallest band dispersion. Additional analysis of the effect of the slab thickness on the interface states is provided in the Supplemental Material [65]. The local density of states, illustrated in Fig. 8, shows that the interface states (purple) are present around the Fermi level only at the interface. Away from the interface, the bulk DOS of InAs (red) and EuS (green) is recovered. Figure 9 shows the partial charges associated with the interface states at the Γ point. The interface configuration also affects the wave function of the interface state: For C1 the interface state wave function is predominantly localized on the EuS side of the interface; for C3 the interface state

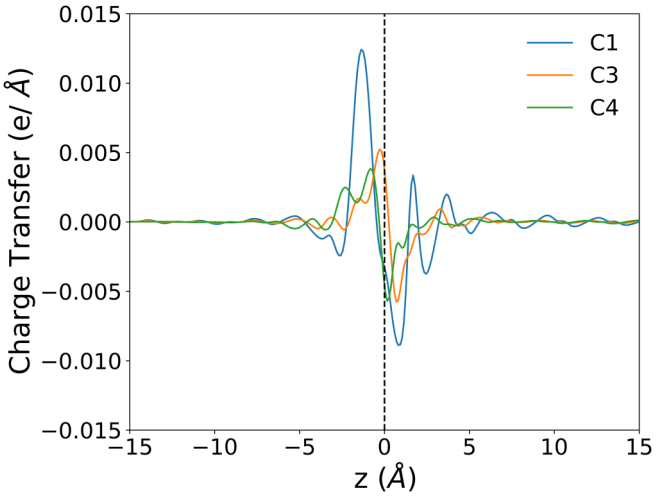

FIG. 10. Charge transfer as a function of distance from the interface for EuS/InAs interfaces with different configurations. The center of the interface is referenced to zero. InAs is on the left side, and EuS is on the right side.

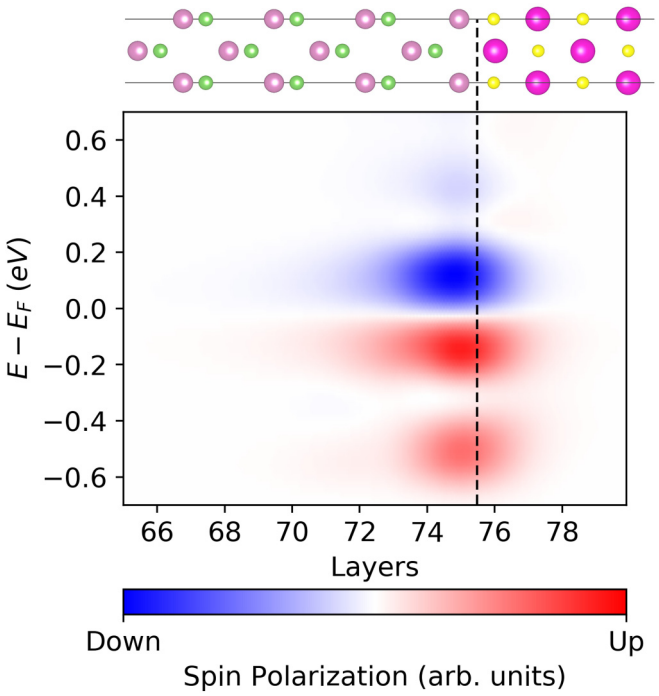

FIG. 11. Spin polarization (the difference between the majority DOS and the minority DOS) as a function of the layer index for C3. Up and down refer to the spin-majority DOS and spin-minority DOS. The position of the interface is indicated by the black dashed line.

wave function is predominantly localized on the InAs side of the interface; and for C4 the interface state wave function is evenly distributed across the InAs and EuS.

The effect of the interface configuration on the band alignment and the dispersion of the interface state may be explained by the extent of charge transfer at the interface. The net charge transfer was calculated by

$$C_{net}(z) = C[\text{interface}] - C[\text{substrate}] - C[\text{film}], \quad (1)$$

where $C[\cdot]$ is the charge averaged over the xy plane along the z axis [41]. The center of the interface is defined as $z = 0$. To evaluate the charge transfer, DFT calculations were performed for the interface slab and for separate slabs containing only the substrate and only the film with the same geometry as the interface slab. Figure 10 shows the resulting charge transfer for different interface configurations. C_{net} is positive at the interfacial layer of InAs and negative at the first layer of EuS, meaning that charge is transferred from the EuS to the InAs. C1 exhibits the greatest charge transfer, followed by C3 and C4. The larger the charge transfer is, the lower the EuS VBM lies below the InAs VBM, and the greater the band dispersion of the interface state is.

The computed magnetic moment of the Eu atoms in bulk EuS is found to be $7.0\,\mu_B$, as expected. However, the proximity-induced magnetic moment in the InAs is small for all three interface configurations. The magnetic moment in the first layer of InAs (the In atom) adjacent to the EuS is $0.013\,\mu_B$ for C1, $0.087\,\mu_B$ for C3, and $0.166\,\mu_B$ for C4. The magnetic moment decays rapidly with the distance from the interface and vanishes completely by the eighth atomic layer of InAs from the interface. The induced magnetic moment is inversely correlated with the extent of charge transfer at the interface. In Ref. [42], a DFT calculation was conducted for a small interface model with two unit cells of each material in C1 and 10 Å of vacuum without surface passivation. PBE+U was used with a U value of 6 eV for the f orbital of Eu. The authors found a magnetic moment of $0.07\,\mu_B$ on the In atom adjacent to the EuS. Despite the small induced magnetic moment, the DOS at the interface is spin polarized, as shown in Fig. 11. About 0.25 eV below the Fermi level the DOS is dominated by the majority-spin channel, whereas the minority-spin channel dominates about 0.2 eV above the Fermi level. This spin polarization is highly localized to the first few InAs layers near the interface—the same region where the dispersed interface states exist. Based on our results, it is difficult to reconcile large effects such as the recent observations of magnetic hysteresis and of zero-bias conductance peaks at zero magnetic field in EuS/InAs/Al hybrid quantum devices [43,44] with proximity-induced magnetic moment in InAs. Other effects, such as EuS/Al magnetic exchange [34,36] and the presence of stray magnetic fields from EuS, could potentially lead to similar signatures and warrant closer investigation. Weakly spin polarized in-plane transport may be possible at the EuS/InAs interface via the interface state.

IV. CONCLUSION

In summary, we have conducted a first-principles investigation of the effect of the bonding configuration on the electronic properties of the EuS/InAs (001) interface, using DFT with a machine-learned Hubbard U correction. The DFT+U(BO) method enables unprecedented simulations of large, well-converged interface models. For all interface configurations studied here, the valence band of EuS lies below the valence band of InAs. In addition, a dispersed interface state appears at the top of the InAs valence band, which is contributed primarily by the InAs layer closest to the interface. These

findings are in agreement with ARPES experiments reported in Ref. [42]. The different interface configurations differ in the band alignment between EuS and InAs and in the dispersion of the interface state. Both are correlated with the extent of charge transfer from EuS to InAs at the interface. The greater the charge transfer is, the lower the EuS VBM lies below the InAs VBM, and the more dispersed the interface state becomes. For all interface configurations studied here, the induced magnetic moment in InAs is found to be modest and spatially confined to the vicinity of the interface, which is also in agreement with Ref. [42]. Our results suggest that EuS/InAs coherent interfaces may not be ideally suited for applications that seek to leverage equilibrium magnetic moments induced in a III-V semiconductor by proximity. This work demonstrates that first-principles simulations may help interpret experimental findings and elucidate the electronic properties as they relate to the interface structure.

ACKNOWLEDGMENTS

We thank P. Krogstrup and Y. Liu from the University of Copenhagen and Microsoft Quantum Materials Lab Copenhagen and S. Martí-Sanchez from the Catalan Institute of Nanoscience and Nanotechnology for helpful discussions on the details of their HAADF-STEM experiments and DFT calculations. We thank S. Frolov from the University of Pittsburgh, P. Crowell from the University of Minnesota, and C. Palmstrøm from the University of California, Santa Barbara, for helpful discussions. This research was funded by the Department of Energy (DOE) through Grant No. DE-SC0019274. This research used resources of the National Energy Research Scientific Computing Center (NERSC), a DOE Office of Science User Facility supported by the Office of Science of the US Department of Energy under Contract No. DE-AC02-05CH11231.

[1] A. Y. Kitaev, Unpaired Majorana fermions in quantum wires, Phys.-Usp. **44**, 131 (2001).

[2] A. Y. Kitaev, Fault-tolerant quantum computation by anyons, Ann. Phys. (NY) **303**, 2 (2003).

[3] S. D. Sarma, M. Freedman, and C. Nayak, Majorana zero modes and topological quantum computation, NPJ Quantum Inf. **1**, 15001 (2015).

[4] R. M. Lutchyn, E. P. A. M. Bakkers, L. P. Kouwenhoven, P. Krogstrup, C. M. Marcus, and Y. Oreg, Majorana zero modes in superconductor–semiconductor heterostructures, Nat. Rev. Mater. **3**, 52 (2018).

[5] C. Nayak, S. H. Simon, A. Stern, M. Freedman, and S. D. Sarma, Non-Abelian anyons and topological quantum computation, Rev. Mod. Phys. **80**, 1083 (2008).

[6] M. Freedman, A. Kitaev, M. Larsen, and Z. H. Wang, Topological quantum computation, Bull. Am. Math. Soc. **40**, 31 (2003).

[7] A. Das, Y. Ronen, Y. Most, Y. Oreg, M. Heiblum, and H. Shtrikman, Zero-bias peaks and splitting in an Al-InAs nanowire topological superconductor as a signature of Majorana fermions, Nat. Phys. **8**, 887 (2012).

[8] J. S. Lee, B. Shojaei, M. Pendharkar, A. P. McFadden, Y. Kim, H. J. Suominen, M. Kjaergaard, F. Nichele, H. Zhang, and C. M. Marcus, Transport Studies of Epi-Al/InAs Two-Dimensional Electron Gas Systems for Required Building-Blocks in Topological Superconductor Networks, Nano Lett. **19**, 3083 (2019).

[9] L. Fu and C. L. Kane, Superconducting Proximity Effect and Majorana Fermions at the Surface of a Topological Insulator, Phys. Rev. Lett. **100**, 096407 (2008).

[10] J. Alicea, Majorana fermions in a tunable semiconductor device, Phys. Rev. B **81**, 125318 (2010).

[11] Y. Oreg, G. Refael, and F. Von Oppen, Helical Liquids and Majorana Bound States in Quantum Wires, Phys. Rev. Lett. **105**, 177002 (2010).

[12] W. Mayer, J. Yuan, K. S. Wickramasinghe, T. Nguyen, M. C. Dartiailh, and J. Shabani, Superconducting proximity effect in epitaxial Al-InAs heterostructures, Appl. Phys. Lett. **114**, 103104 (2019).

[13] R. M. Lutchyn, J. D. Sau, and S. D. Sarma, Majorana Fermions and a Topological Phase Transition in Semiconductor-Superconductor Heterostructures, Phys. Rev. Lett. **105**, 077001 (2010).

[14] H. Y. Günel, I. E. Batov, H. Hardtdegen, K. Sladek, A. Winden, K. Weis, G. Panaitov, D. Grützmacher, and T. Schäpers, Supercurrent in Nb/InAs-nanowire/Nb Josephson junctions, J. Appl. Phys. **112**, 034316 (2012).

[15] N. A. Güsken, T. Rieger, P. Zellekens, B. Bennemann, E. Neumann, M. I. Lepsa, T. Schäpers, and D. Grützmacher, MBE growth of Al/InAs and Nb/InAs superconducting hybrid nanowire structures, Nanoscale **9**, 16735 (2017).

[16] J. Paajaste, M. Amado, S. Roddaro, F. S. Bergeret, D. Ercolani, L. Sorba, and F. Giazotto, Pb/InAs nanowire Josephson junction with high critical current and magnetic flux focusing, Nano Lett. **15**, 1803 (2015).

[17] M. T. Deng, C. L. Yu, G. Y. Huang, M. Larsson, P. Caroff, and H. Q. Xu, Anomalous zero-bias conductance peak in a Nb-InSb nanowire-Nb hybrid device, Nano Lett. **12**, 6414 (2012).

[18] W. Y. He, B. T. Zhou, J. J. He, N. F. Q. Yuan, T. Zhang, and K. T. Law, Magnetic field driven nodal topological superconductivity in monolayer transition metal dichalcogenides, Commun. Phys. **1**, 40 (2018).

[19] M. Leijnse and K. Flensberg, Introduction to topological superconductivity and Majorana fermions, Semicond. Sci. Technol. **27**, 124003 (2012).

[20] Z. D. Yang, B. Heischmidt, S. Gazibegovic, G. Badawy, D. Car, P. A. Crowell, E. P. A. M. Bakkers, and V. S. Pribiag, Spin Transport in Ferromagnet-InSb Nanowire Quantum Devices, Nano Lett. **20**, 3232 (2020).

[21] Y. Jiang, E. J. De Jong, V. van de Sande, S. Gazibegovic, G. Badawy, E. P. A. M. Bakkers, and S. M. Frolov, Hysteretic magnetoresistance in nanowire devices due to stray fields induced by micromagnets, Nanotechnology **32**, 095001 (2020).

[22] J. D. Sau, S. Tewari, R. M. Lutchyn, T. D. Stanescu, and S. D. Sarma, Non-Abelian quantum order in spin-orbit-coupled semiconductors: Search for topological Majorana particles in solid-state systems, Phys. Rev. B **82**, 214509 (2010).

[23] C. Adelmann, X. Lou, J. Strand, C. J. Palmstrøm, and P. A. Crowell, Spin injection and relaxation in ferromagnet-semiconductor heterostructures, Phys. Rev. B **71**, 121301(R) (2005).

[24] X. H. Lou, C. Adelmann, S. A. Crooker, E. S. Garlid, J. J. Zhang, K. S. M. Reddy, S. D. Flexner, C. J. Palmstrøm, and P. A. Crowell, Electrical detection of spin transport in lateral ferromagnet–semiconductor devices, Nat. Phys. **3**, 197 (2007).

[25] H. J. Zhu, M. Ramsteiner, H. Kostial, M. Wassermeier, H. P. Schönherr, and K. H. Ploog, Room-Temperature Spin Injection from Fe into GaAs, Phys. Rev. Lett. **87**, 016601(R) (2001).

[26] S. F. Alvarado and P. Renaud, Observation of Spin-Polarized-Electron Tunneling from a Ferromagnet into GaAs, Phys. Rev. Lett. **68**, 1387 (1992).

[27] A. T. Hanbicki, B. T. Jonker, G. Itskos, G. Kioseoglou, and A. Petrou, Efficient electrical spin injection from a magnetic metal/tunnel barrier contact into a semiconductor, Appl. Phys. Lett. **80**, 1240 (2002).

[28] A. Fert and H. Jaffres, Conditions for efficient spin injection from a ferromagnetic metal into a semiconductor, Phys. Rev. B **64**, 184420 (2001).

[29] J. D. Sau, R. M. Lutchyn, S. Tewari, and S. D. Sarma, Generic New Platform for Topological Quantum Computation Using Semiconductor Heterostructures, Phys. Rev. Lett. **104**, 040502 (2010).

[30] P. Wei, S. Lee, F. Lemaitre, L. Pinel, D. Cutaia, W. Cha, F. Katmis, Y. Zhu, D. Heiman, and J. Hone, Strong interfacial exchange field in the graphene/EuS heterostructure, Nat. Mater. **15**, 711 (2016).

[31] F. Katmis, V. Lauter, F. S. Nogueira, B. A. Assaf, M. E. Jamer, P. Wei, B. Satpati, J. W. Freeland, I. Eremin, and D. Heiman, A high-temperature ferromagnetic topological insulating phase by proximity coupling, Nature (London) **533**, 513 (2016).

[32] H. Q. Chen, B. Li, and J. L. Yang, Proximity effect induced spin injection in phosphorene on magnetic insulator, ACS Appl. Mater. Interfaces **9**, 38999 (2017).

[33] X. Liang, L. J. Deng, F. Huang, T. T. Tang, C. T. Wang, Y. P. Zhu, J. Qin, Y. Zhang, B. Peng, and L. Bi, The magnetic proximity effect and electrical field tunable valley degeneracy in MoS_2/EuS van der Waals heterojunctions, Nanoscale **9**, 9502 (2017).

[34] J. S. Moodera, X. Hao, G. A. Gibson, and R. Meservey, Electron-Spin Polarization in Tunnel Junctions in Zero Applied Field with Ferromagnetic EuS Barriers, Phys. Rev. Lett. **61**, 637 (1988).

[35] B. Li, N. Roschewsky, B. A. Assaf, M. Eich, M. Epstein-Martin, D. Heiman, M. Münzenberg, and J. S. Moodera, Superconducting Spin Switch with Infinite Magnetoresistance Induced by an Internal Exchange Field, Phys. Rev. Lett. **110**, 097001 (2013).

[36] Y. M. Xiong, S. Stadler, P. W. Adams, and G. Catelani, Spin-Resolved Tunneling Studies of the Exchange Field in EuS/Al Bilayers, Phys. Rev. Lett. **106**, 247001 (2011).

[37] S. Diesch, P. Machon, M. Wolz, C. Sürgers, D. Beckmann, W. Belzig, and E. Scheer, Creation of equal-spin triplet superconductivity at the Al/EuS interface, Nat. Commun. **9**, 5248 (2018).

[38] J. M. Gomez-Perez, X. P. Zhang, F. Calavalle, M. Ilyn, C. Gonzlez-Orellana, M. Gobbi, C. Rogero, A. Chuvilin, V. N. Golovach, L. E. Hueso, F. S. Bergeret, and F. Casanova, Strong interfacial exchange field in a heavy metal/ferromagnetic insulator system determined by spin Hall magnetoresistance, Nano Lett. **20**, 6815 (2020).

[39] B. A. Assaf, F. Katmis, P. Wei, C. Z. Chang, B. Satpati, J. S. Moodera, and D. Heiman, Inducing magnetism onto the surface of a topological crystalline insulator, Phys. Rev. B **91**, 195310 (2015).

[40] Q. I. Yang and A. Kapitulnik, Two-stage proximity-induced gap opening in topological-insulator–insulating-ferromagnet $(Bi_xSb_{1-x})_2Te_3$–EuS bilayers, Phys. Rev. B **98**, 081403(R) (2018).

[41] S. Y. Yang, C. Z. Wu, and N. Marom, Topological properties of SnSe/EuS and SnTe/CaTe interfaces, Phys. Rev. Mater. **4**, 034203 (2020).

[42] Y. Liu, A. Luchini, S. Martí-Sánchez, C. Koch, S. Schuwalow, S. A. Khan, T. Stankevic, S. Francoual, J. R. L. Mardegan, J. A. Krieger, V. N. Strocov, J. Stahn, C. A. F. Vaz, M. Ramakrishnan, U. Staub, K. Lefmann, G. Aeppli, J. Arbiol, and P. Krogstrup, Coherent Epitaxial Semiconductor–Ferromagnetic Insulator InAs/EuS Interfaces: Band Alignment and Magnetic Structure, ACS Appl. Mater. Interfaces **12**, 8780 (2020).

[43] Y. Liu, S. Vaitiekėnas, S. Martí-Sánchez, C. Koch, S. Hart, Z. Cui, T. Kanne, S. A. Khan, R. Tanta, S. Upadhyay, M. E. Cachaza, C. M. Marcus, J. Arbiol, K. A. Moler, and P. Krogstrup, Semiconductor-ferromagnetic insulator-superconductor nanowires: Stray field and exchange field, Nano Lett. **20**, 456 (2020).

[44] S. Vaitiekėnas, Y. Liu, P. Krogstrup, and C. M. Marcus, Zero-bias peaks at zero magnetic field in ferromagnetic hybrid nanowires, Nat. Phys. **17**, 43 (2021).

[45] J. P. Perdew, K. Burke, and M. Ernzerhof, Generalized Gradient Approximation Made Simple, Phys. Rev. Lett. **77**, 3865 (1996).

[46] M. T. Yu, S. Y. Yang, C. Z. Wu, and N. Marom, Machine learning the Hubbard U parameter in DFT+ U using Bayesian optimization, npj Comput. Mater. **6**, 180 (2020).

[47] D. B. Ghosh, M. De, and S. K. De, Electronic structure and magneto-optical properties of magnetic semiconductors: Europium monochalcogenides, Phys. Rev. B **70**, 115211 (2004).

[48] P. Wachter, The optical electrical and magnetic properties of the europium chalcogenides and the rare earth pnictides, Crit. Rev. Solid State Mater. Sci. **3**, 189 (1972).

[49] S. Massidda, A. Continenza, A. J. Freeman, T. M. De Pascale, F. Meloni, and M. Serra, Structural and electronic properties of narrow-band-gap semiconductors: InP, InAs, and InSb, Phys. Rev. B **41**, 12079 (1990).

[50] Y. S. Kim, K. Hummer, and G. Kresse, Accurate band structures and effective masses for InP, InAs, and InSb using hybrid functionals, Phys. Rev. B **80**, 035203 (2009).

[51] M. Schlipf, M. Betzinger, M. Ležaić, C. Friedrich, and S. Blügel, Structural, electronic, and magnetic properties of the europium chalcogenides: A hybrid-functional DFT study, Phys. Rev. B **88**, 094433 (2013).

[52] V. I. Anisimov, J. Zaanen, and O. K. Andersen, Band theory and Mott insulators: Hubbard U instead of Stoner I, Phys. Rev. B **44**, 943 (1991).

[53] S. L. Dudarev, G. A. Botton, S. Y. Savrasov, C. J. Humphreys, and A. P. Sutton, Electron-energy-loss spectra and the structural stability of nickel oxide: An LSDA+U study, Phys. Rev. B **57**, 1505 (1998).

[54] S. Y. Yang, N. Schröter, S. Schuwalow, M. Rajpalk, K. Ohtani, P. Krogstrup Georg, W. Winkler, J. Gukelberger, D. Gresch,

and G. Aeppli, Electronic structure of InAs and InSb surfaces: Density functional theory and angle-resolved photoemission spectroscopy, arXiv:2012.14935 (2020).

[55] S. Y. Yang, D. Dardzinski, A. Hwang, D. I. Pikulin, G. W. Winkler, and N. Marom, First principles feasibility assessment of a topological insulator at the InAs/GaSb interface, arXiv:2101.07873 (2021).

[56] R. T. Tung, The physics and chemistry of the Schottky barrier height, Appl. Phys. Rev. **1**, 011304 (2014).

[57] G. Kresse and J. Hafner, *Ab initio* molecular dynamics for liquid metals, Phys. Rev. B **47**, 558 (1993).

[58] G. Kresse and D. Joubert, From ultrasoft pseudopotentials to the projector augmented-wave method, Phys. Rev. B **59**, 1758 (1999).

[59] P. E. Blöchl, Projector augmented-wave method, Phys. Rev. B **50**, 17953 (1994).

[60] S. Steiner, S. Khmelevskyi, M. Marsmann, and G. Kresse, Calculation of the magnetic anisotropy with projected-augmented-wave methodology and the case study of disordered $Fe_{1-x}Co_x$ alloys, Phys. Rev. B **93**, 224425 (2016).

[61] J. Neugebauer and M. Scheffler, Adsorbate-substrate and adsorbate-adsorbate interactions of Na and K adlayers on Al (111), Phys. Rev. B **46**, 16067 (1992).

[62] A. Tkatchenko and M. Scheffler, Accurate Molecular van der Waals Interactions from Ground-State Electron Density and Free-Atom Reference Data, Phys. Rev. Lett. **102**, 073005 (2009).

[63] D. Colleoni, G. Miceli, and A. Pasquarello, Band Alignment and Chemical Bonding at the $GaAs/Al_2O_3$ Interface: A Hybrid Functional Study, Appl. Phys. Lett. **107**, 211601 (2015).

[64] L. Colombo, R. Resta, and S. Baroni, Valence-Band Offsets at Strained Si/Ge Interfaces, Phys. Rev. B **44**, 5572 (1991).

[65] See Supplemental Material at http://link.aps.org/supplemental/10.1103/PhysRevMaterials.5.064606 for additional calculations of the valence band offsets using the macroscopic averaging procedure and additional analysis of the effect of the slab thickness on the interface states.